Macromolecules
ARTICLE

Formation of Oriented, Suspended Fibers by Melting Free Standing Polystyrene Thin Films

Jeremy M. Rathfon, Joshua M. Grolman, Alfred J. Crosby, and Gregory N. Tew*

Department of Polymer Science and Engineering, University of Massachusetts Amherst, 120 Governors Drive, Amherst, Massachusetts 01003

ABSTRACT: A new approach toward the fabrication of oriented, suspended fibers from the melting of free-standing polymer thin films is presented. Thin films (between 35 and 120 nm) cast via flow coating are melted atop lithographically patterned arrays of pillars to form suspended fibers (from ~2 to 3 μm in diameter) between pillars. The effects of film thickness and pillar spacing on fiber diameter and yield are probed in a combinatorial fashion. A novel image analysis technique for the acquisition of fiber diameter across the multivariable parameter space is also outlined. This thin film melting approach details a new technique toward the fabrication of oriented, suspended micro and nanofiber networks with specific point to point connections in desired architectures.

Introduction

In recent years, there has been a growing interest in the fabrication of polymeric micro- and nanofibers due to their potential use for device applications in nanoelectronics,[1-3] optical sensors,[4-6] and nano-optics.[7,8] These applications require the ability to fabricate fibers with regular diameters and orientation in two and three-dimensional architectures with point-to-point connections. Many approaches have been developed for the fabrication of ordered polymeric nanofibers, including self-assembly/directed assembly,[9-11] template synthesis,[12-14] electrospinning,[15-23] and various drawing techniques;[24-30] the most popular is electrospinning due to its ability to produce micro- to nanoscale fibers in a facile, continuous fashion. However, common difficulties encountered in these approaches include random fiber alignment, nonuniformity in fiber diameter, and upscaling problems.[21,24,26,28] Besides overcoming these difficulties, fabrication of controlled, interconnected networks of one, two, and three-dimensional nanofibers has proven to be challenging. Precisely positioned micro- and nanoscale fibers are highly desired for their potential integration into nanoscale devices such as microelectromechanical systems (MEMS), nanoelectronics, and nano-optics.

Harfenist et al. have developed an approach toward the fabrication of suspended, polymer fibers using a direct drawing technique, where an applicator sheet coated with a viscous polymer solution is drawn across a patterned array of pillars.[25] This "direct drawing" fabrication technique has proven to be useful in the formation of oriented, parallel arrays of suspended fibers from 50 nm to several micrometers in diameter, yet improvements can still be made. This drawing technique requires the polymer solution to be in the highly concentrated regime and is dependent on mass transfer, due to solvent evaporation, for the formation and thinning of fibers which makes fiber properties difficult to control. The ability to control parameters such as fiber diameter, orientation, polymer composition, and morphology across an array of nanofibers would allow the fabrication of more complex three-dimensional architectures and thus a larger range of devices.

In this report, a novel approach is presented for the fabrication of oriented, suspended fibers in interconnected networks with control over parameters such as fiber diameter and the patterning of the substrate. Polymer thin films with a controlled, gradient thickness (~20−120 nm) are suspended from lithographically patterned substrates comprised of microscale pillar arrays. The films are annealed above the glass transition temperature (T_g) forming polymer fibers suspended between the patterned pillars. The resultant fiber diameter can be controlled by tuning the parent film thickness and the pillar spacing. Moreover, by orthogonally combining gradient thickness films with various pillar spacings a combinatorial landscape is provided which allows these two parameters to be rapidly explored. This thin film melting approach represents the initial developments toward fabrication of suspended micro and nanofiber networks with specific two-dimensional architectures in three-dimensional devices. Applications could be envisioned where pillar arrays with electrode or optical tips are utilized for the direct addressing of individual fibers from this film melting approach.

A general scheme for the formation of fibers via thin film melting is presented in Figure 1. In this approach a gradient thickness, polymer thin film is cast onto a silicon wafer utilizing the "flow coating"[31] technique. The thin film is separated from the substrate by floating the film onto water, from which it can be picked up and transferred onto a lithographically patterned array of pillars. The now suspended film is thermally annealed above the T_g to form suspended, oriented fibers. A representative optical microscopy (OM) image of the resulting fibers (~15 μm in length and ~2 μm in diameter) is also shown. Data analysis is performed on images of pillar arrays, and trends of fiber diameter as a function of parent film thickness and pillar spacing are investigated.

Results and Discussion

Thin Film Preparation. The technique of flow coating was developed to fabricate polymer thin films with controlled thickness gradients in the submicrometer to nanoscale regime.[31] These films were used for combinatorial, high-throughput analysis of thin film thickness effects on phenomena such as block copolymer morphology,[32,33] polymer

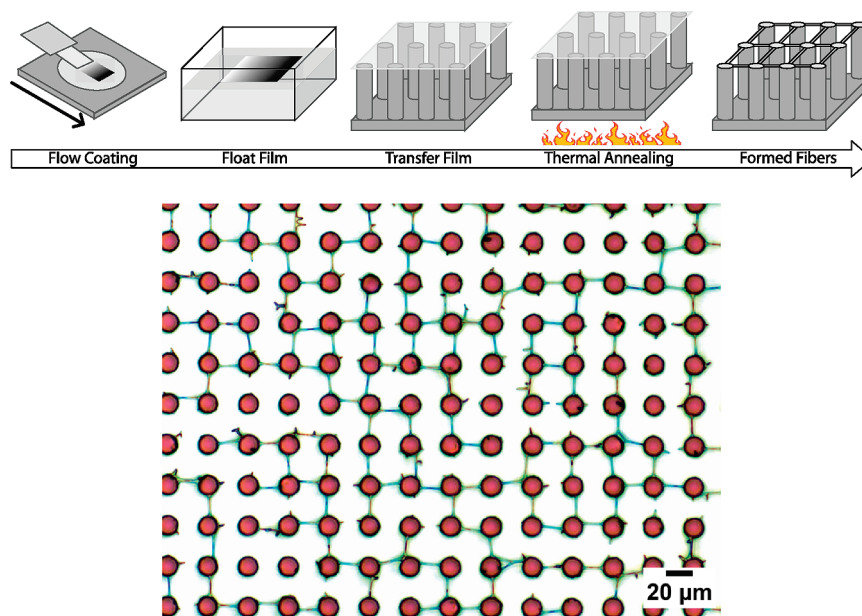*Corresponding author. E-mail: tew@mail.pse.umass.edu.

Figure 1. Experimental approach for fiber formation via flow coating and thin film melting, with a representative fiber image shown.
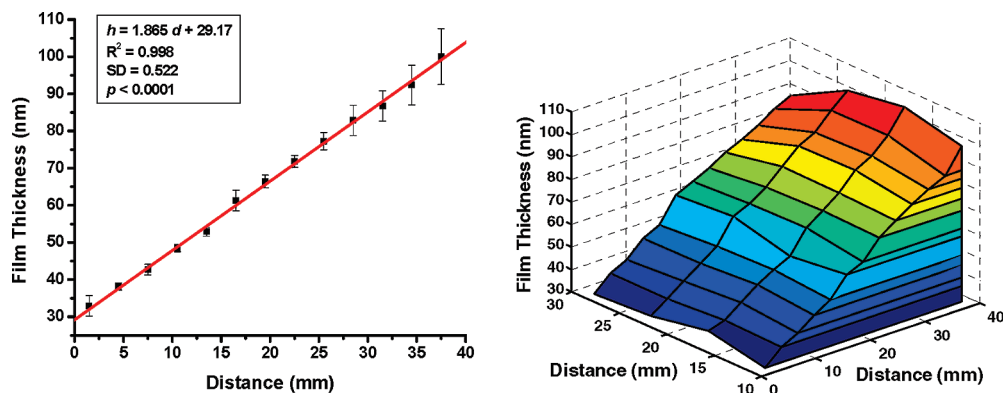

Figure 2. (Left) Film thickness versus distance for a representative gradient thickness film placed atop a multiple pillar spacing array. (Right) Film thickness surface plot for the same film measured via UV–visible interferometry.

blend phase behavior,[34] dewetting,[35,36] and crazing/fracture.[37,38] Stafford et al. thoroughly outlined how to create gradient thickness polymer thin films of desired scale by varying parameters including stage velocity and acceleration, concentration and volume of polymer solutions, as well as device geometry.[31] Films in this study were created with gradient thicknesses using an acceleration of 6 mm/s^2 and varying the concentration of polystyrene (PS) solution: 2.0 wt % PS ($M_n = 400$ kDa) in toluene for films between 60 and 120 nm and 1.5 wt % for films between 30 and 80 nm. A representative film thickness profile and surface plot are given in Figure 2. Once a thin film was prepared on a silicon wafer, it was floated onto a previously fabricated pillar array by lowering the wafer into a water bath which separates the film from the water and floats it onto the surface of the water. A pillar array is then inserted under the film and lifted to pull the film from the surface of the water. The gradient in film thickness is placed orthogonally to the varied spacings of the arrays giving a two-dimensional parameter space.

Fiber Formation. Thin films were thermally annealed at 150 °C, above the T_g (PS ∼ 100 °C) of the bulk polymer (Figure 3). As the polymer film begins to melt, the melt viscosity decreases until instabilities occur in the film, causing holes to form. Brenn et al. studied the stability of viscoelastic sheets in detail, and showed that viscosity and surface tension tend to stabilize the sheet while elasticity enhances sheet instability.[39] Holes form by two mechanisms in freely standing polymer thin films from the melt state: either spontaneously in a process analogous to spinodal decomposition[40,41] or by nucleation from defects such as dust (< 0.2 μm) or density inhomogeneities. Holes observed in this report formed spontaneously in the melt in random locations consistent with literature findings[41–43] (see Figure S1) and not at the pillar edges.[44–46]

Although not the focus of this study, because holes lead directly to fiber formation, some discussion of their formation and growth is presented. The growth of holes in free-standing thin films has been studied in detail by Debrégas et al. in thick (5–50 μm) PDMS films[47,48] and thin (60–500 nm) PS films.[41–43] In our study, annealing temperatures were well above bulk T_g for PS, thus hole growth is expected to be exponential according to the literature (see movie, available as Supporting Information). The formed holes expand via surface tension driven capillary forces exerted from the film and eventually are impinged by pillars or other holes in the film. Where the hole edges meet, bridges are formed between the pillars of the array. These bridges thin over time due to capillary forces to create suspended fibers
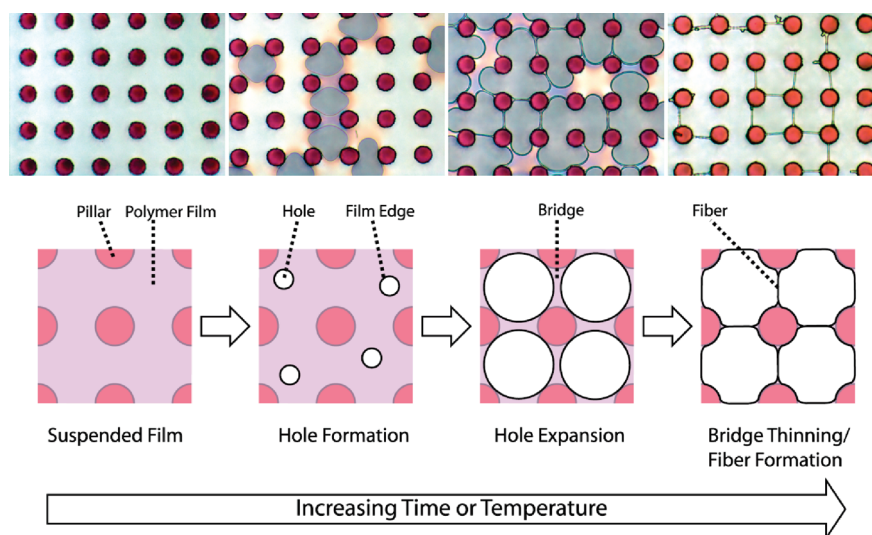
Figure 3. Fiber formation from the annealing of free-standing PS thin films. Images are taken at different areas of the same film after successive heating cycles.

between the pillars (see right most side of Figure 3). The thinning, or necking, of these fibers is either slowed by an increased melt viscosity, a result of strain-hardening of the polymer melt,[49,50] or by simply cooling the array below the T_g, thus quenching the fiber formation.

The temperature and annealing time are critical factors in fiber formation; the melt viscosity is inversely proportional to temperature given by the empirical Williams−Landau−Ferry (WLF) equation. Films annealed at too low of a temperature or too short a time will not sufficiently melt; whereas, films annealed at too high a temperature or too long a time result in fibers that have thinned too far and snapped. The orientation of fibers is directly affected by the pillar array geometry, whereas the diameter is affected both by the preceding film thickness and the pillar array geometry; a larger distance between pillars results in more material per fiber.

Data Acquisition via Image Analysis. In order to efficiently analyze the vast amount of data created from this combinatorial approach toward fiber fabrication, data acquisition was automated as manual acquisition takes an immeasurable amount of time. On the basis of recent techniques developed for measuring electrospun fiber diameters,[51−53] a more versatile image analysis method was developed for the measurement of fibers suspended on pillar arrays. In this method, images of fibers (Figure 4a) are converted to binary images of 0's and 1's (black and white, respectively, Figure 4b) where 0's are nonobject pixels and 1's correspond to objects. A Euclidean distance calculation is performed on the binary images, where every pixel value is converted to a distance value based on its distance to a zero pixel. This creates an image called a "distance map" (color enhanced in Figure 4c) where the pixel values correspond to the distance to the edge of a fiber (hot colors represent larger distances). The binary image is also used to create a "skeleton" where objects are represented as traces that are one-pixel in width, located at the center of the corresponding objects. Pillars appear as connected objects in the binary images and therefore they must be removed in order to analyze the fibers. Multiple sliding neighborhood operations,[54] have been developed and employed for this task, which systematically remove pixels associated with large objects in a skeleton, resulting in an image of only desired objects, corresponding to fibers.[55] Sliding neighborhood operations also remove spurs, junctions

(thus separating fibers), and other discontinuities in the skeletonized image (Figure 4d). This pruned and cleaned skeleton is multiplied element-by-element to the distance map in order to calculate individual fiber diameters, thus the distribution of fiber diameters per image can be determined (Figure 4e). These image values are compiled to observe trends across an array in which parameters such as film thickness or pillar spacing are varied.

Analysis of Fiber Properties. In this report, parent film thickness and pillar spacing were varied in order to better understand their effects on fiber diameter and yield. Both film thickness h, and post spacing d, will directly affect fiber diameter. The volume of a fiber is approximately equal to the length, the pillar spacing d, times its cross-sectional area, πr^2, where r is the radius. The volume of a polymer film between pillars in a square array is given by the thickness h, multiplied by the area, d^2. Assuming the polymer in a unit cell melts into two uniform fibers, the fiber volume and film volume are roughly equal, thus a relationship for the fiber diameter versus pillar spacing can be derived as shown:

$$2\pi r^2 d \cong d^2 h \tag{1}$$

$$\text{diameter} = 2r \cong (2hd/\pi)^{1/2} \tag{2}$$

This relationship shows that fiber diameter is proportional to the square root of both film thickness and pillar spacing. As the film thickness increases or the spacing between posts becomes larger, more volume of polymer is available for fiber formation, thus the resultant fiber diameter is expected to be larger.

Data was collected to verify the relationship between the resultant fiber diameter and the parent thin film thickness, holding the pillar spacing constant. Figure 5 shows fiber diameter values (1.97 to 2.77 μm) for PS thin films with a range of film thicknesses from ~35 to 120 nm. Regression using the previously described volume balance (eq 1, while allowing for volume of polymer atop pillars) with weight given by error was performed, exhibiting a dependence of fiber diameter on film thickness ($R^2 = 0.923$, $\chi^2/\text{DoF} = 0.00114$), shown by the fitting curve in Figure 5. Performing analysis of variance (ANOVA) tests confirms that fiber diameter is in fact dependent upon film thickness with a high
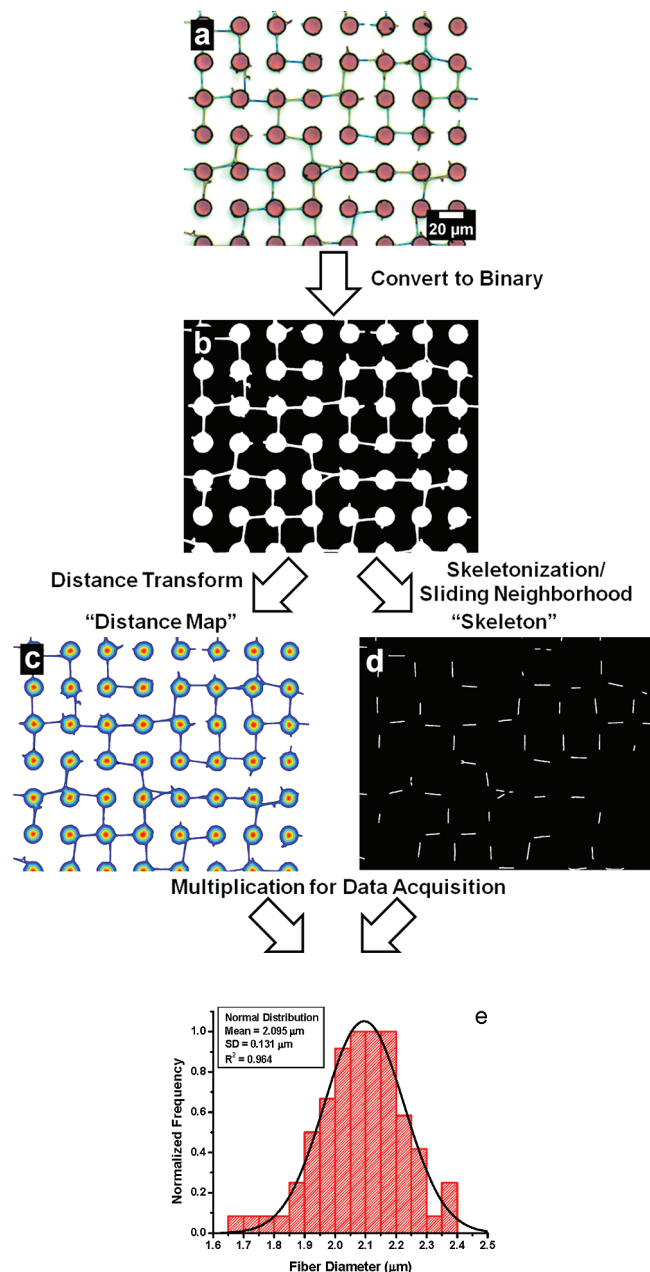
Figure 4. Schematic of the image analysis performed on OM fiber images. (a) Fiber image, (b) converted binary image, (c) distance transform of binary image, (d) skeletonized and pruned image, and (e) resultant histogram of fiber diameters generated from the element-by-element multiplication of the distance map and the skeleton.

certainty ($p < 0.0001$), and the fiber diameter is proportional to the square root of film thickness, as can be seen in Figure 5.

The geometry of the pillar arrays has a large impact on fiber properties such as diameter, orientation, and yield. As discussed above, fiber diameter is expected to be proportional to the square root of pillar spacing. Gradient thickness thin films ($\sim$50−90 nm) were cast on an array containing regions with pillar spacings of 15, 25, and 35 μm, with pillars $\sim$15 μm in diameter. Representative images of fibers with these three different pillar spacings are shown in Figure 6, parts a, b, and c, respectively. If the controlled variables, film thickness and pillar spacing, are used with the scaling relationship discussed earlier ($2r \cong (2hd/\pi)^{1/2}$), the expected fiber diameter ($2r$) can be calculated. When the measured fiber diameter is plotted versus the calculated fiber diameter,
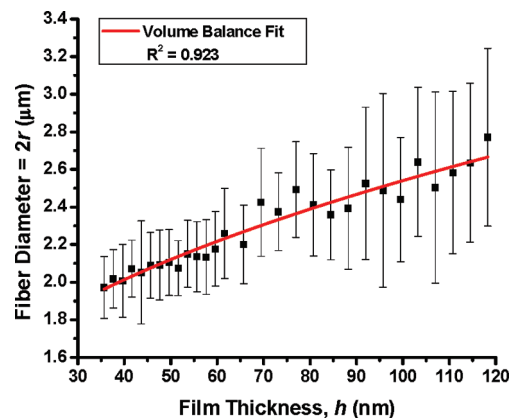

Figure 5. Fiber diameter versus film thickness for a pillar spacing of 15 μm.

a relationship can be determined which is expected to be linear with a slope of one (Figure 6d), independent of pillar spacing. The fiber diameter values do indeed fit a linear trend versus the calculated diameter values ($R^2 = 0.897$, $\sigma^2 = 0.108$, $p < 0.0001$). The calculated slope is 0.895 which deviates slightly from the expected slope of one, but this can be attributed to yield effects versus film thickness and pillar spacing as discussed next.

The effect of film thickness and pillar spacing on yield of fibers was studied (Figure 7). Upon nucleation, holes expand then impinge upon pillars and other holes. Thus the yield of fibers is directly proportional to the number of nucleated holes. If the pillar spacing is increased for a given number of nucleated holes, there would be a larger number of holes per area between pillars, thus the fiber yield increases. This trend can be seen in Figure 7 for data collected from pillar spacings of 15, 25, and 35 μm.

As previously discussed, nucleation can occur via a process analogous to spinodal decomposition. Long-range van der Waals interactions result in attractive forces which bring the two surfaces of the thin film together to form a hole that grows due to surface tension.[42,47] The process is a free energy balance, involving surface tension, between the minimization of energy from viscous dissipation within the film ($\dot{E}_{kin}(R) = 4\pi\eta h\dot{R}^2$, where R is the radius at the hole edge, $\dot{R}$ is the velocity of hole edge) versus the gain in surface energy of the thin film ($\dot{E}_{surf}(R) = (2\gamma)2\pi R\dot{R}$, where γ is the surface energy of the polymer).[42,48] Thus the nucleation of holes can be related to film thickness; as film thickness increases nucleation will decrease.[40,56,57] Because the number of nucleated holes is proportional to yield, the fiber yield is also thickness dependent. For a given pillar spacing, fiber yield decreases as film thickness increases, as shown in Figure 7. The trend in yield versus film thickness can help explain why the measured fiber diameters are larger than eq 2 predicts as shown in Figure 6d. A yield less than 100% results in more volume available per fiber, therefore the resultant fiber diameters must be larger.

Conclusions

A detailed approach toward the fabrication of oriented, suspended fibers from thin film melting is presented. Polystyrene thin films cast via flow coating are suspended atop lithographically patterned arrays of pillars then heated above the T_g. Holes form in the film via random nucleation, which expand exponentially until impingement upon other holes or pillars. These hole edges meet to form fiber bridges which draw over time into suspended fibers between pillars. The effect of both parent film thickness and pillar spacing on resultant fiber diameter and yield
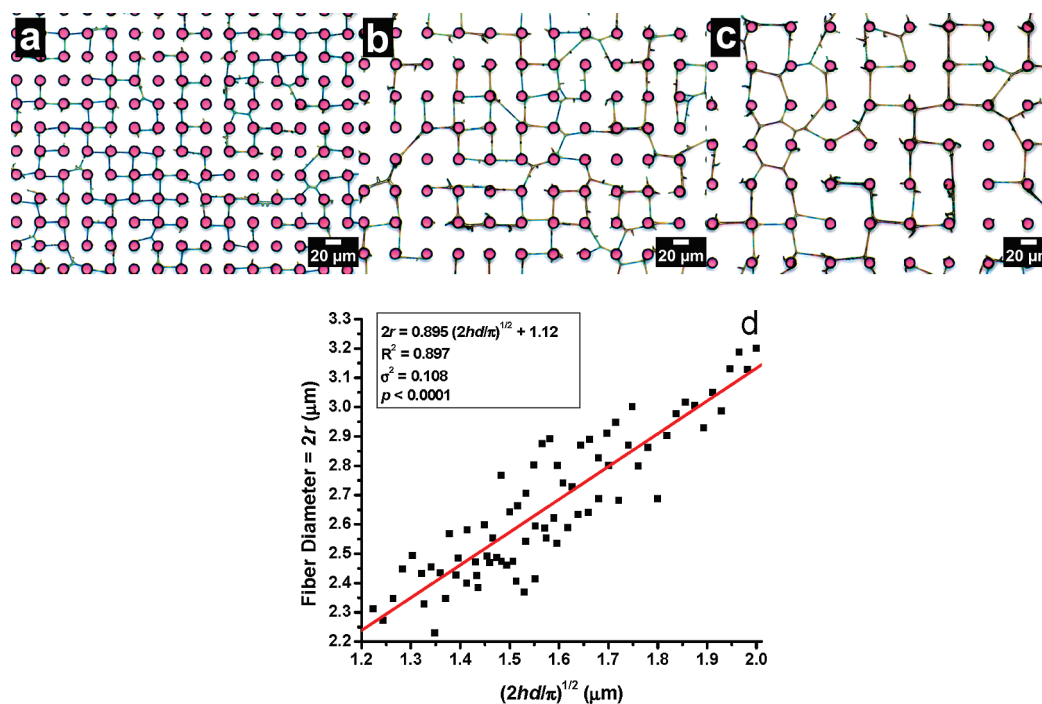
Figure 6. Images of fibers at different pillar spacings: (a) 15, (b) 25, and (c) 35 μm, with parent film thicknesses of ~45, 60, and 65 nm, respectively. (d) Fiber diameter ($2r$) versus the scaling parameter $(2hd/\pi)^{1/2}$.
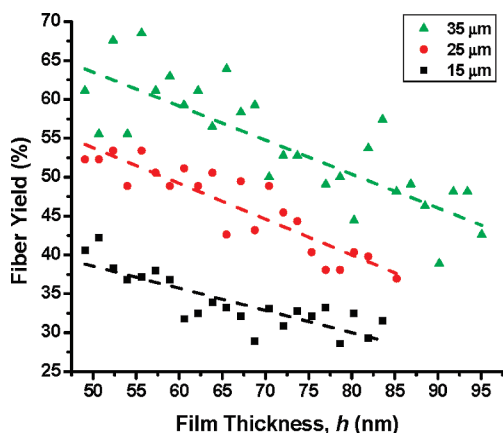
In the plot (d):

$2r = 0.895 (2hd/\pi)^{1/2} + 1.12$
$R^2 = 0.897$
$\sigma^2 = 0.108$
$p < 0.0001$

Figure 7. Yield versus film thickness for a film suspended over an array with varied pillar spacings (15, 25, 35 μm). Dashed lines shown for visual guide.

were probed. Film thickness was varied from 35 to 120 nm. On a separate sample, film thickness was varied between 50 and 100 nm, while in an orthogonal direction three different pillar spacings, 15, 25, and 35 μm, were explored, illustrating a combinatorial approach toward the investigation of fiber properties. The resultant fiber diameter scaled with a volume balance for both film thickness and pillar spacing, whereas yield was directly dependent on the number of holes generated during the nucleation event. This thin film melting approach outlines a new technique toward the fabrication of oriented, suspended micro and nanofiber networks with specific two-dimensional architectures that could be implemented into three-dimensional devices. Future explorations in this technique will look at ultrathin film (< 20 nm) and molecular weight effects on the formation of fibers.

Experimental Section

Pillar Array Fabrication. Pillar arrays are fabricated by photolithography of SU8 (MicroChem Corp., Newton, MA)

negative tone photoresist on polished silicon wafers. SU-8 100 was diluted to 80 wt % with a filtered, saturated solution of rhodamine 6G in γ-butyrolactone. The resist was spun onto silicon wafers to 500 at 100 rpm/s for 5 s then to 2000 at 300 rpm/s for 30 s. The resist was prebaked for 5 min at 65 °C, then soft-baked for 15 min at 95 °C. The wafers were exposed to 365 nm UV light for 40 s at ~ 40 mJ/cm². Gradient pillar spacing array masks were designed in AutoCAD with pillar diameters of 15 μm and spacings of 15, 25, and 35 μm. Transparency masks were printed by CAD/Art Services, Inc. at 20 000 dpi. Wafers were post exposure baked for 1 min at 65 °C, then 4 min at 95 °C. The samples were developed in MicroChem SU-8 Developer for 3.5 min. Completed pillar arrays were hard baked at 190 °C overnight. Representative optical profilometry height profiles of the 15 μm spaced pillar array are given in the Supporting Information, Figure S2; images were taken with a Zygo NewView 7300 Optical Profilometer using 10× and 50× objectives.

Film Preparation and Annealing. Monodisperse polystyrene (PS, $M_n = 400$ kDa, $M_w/M_n = 1.06$, Alfa Aesar) was dissolved in toluene at various concentrations (1.0−2.0 wt %) and filtered through a 40 μm PTFE filter. Before casting, polished silicon wafers were cleaned with acetone and toluene, then UV ozone for 20 min. Thin films were cast onto silicon wafers utilizing the flow coating technique.[31] A bead of PS solution (~50 μL) was cast under the blade. The blade was lowered to a gap height of 300 μm and was drawn across the surface of the wafer, leaving a film of PS solution. The solution evaporates in air to leave a uniform thin film of PS. Variable thickness films were cast at an acceleration of 6 mm/s² starting at 0 velocity for 45 mm. The thickness of cast PS films was measured via a UV−visible interferometer (Model F20, Filmetrics, Inc.) operated in reflectance mode with a spot size of ~0.5 mm. Typical film thickness gradients were ~60−120 nm for 2.0 wt % solutions. Films were floated onto water by lowering the wafer into a bath, whereupon the thin film would separate from the surface. A pillar array was inserted under the floating film and lifted to pull the film

from the surface of the water onto the pillar array. The transferred film on the pillar array was dried overnight at 50 °C under vacuum. Films were annealed at 150 °C for 30 min then pulled from the oven to cool to room temperature.

Image Acquisition and Analysis. OM images were taken with a Zeiss Axioskop 40 A Pol microscope equipped with an AxioCam MRc5 camera at 20× magnification. Abutting images were taken across a sample space in order to obtain data points corresponding to the gradient film thickness. Images were processed using the image analysis procedure developed in MATLAB (see Supporting Information). First, images were converted to binary using an adjusted automatic thresholding command. A Euclidean distance transform was applied to this image to generate a "distance map". In a separate process the binary image was skeletonized to a set number of iterations. A pruning algorithm was applied to remove spurs. Sliding neighborhood operations were developed to remove intersections and larger nonfiber objects. Finally, a size exclusion filter was applied to remove errant pixels, broken fibers, and other noise. The resultant skeletonized image contains only skeletons of complete fibers, with no pillars, represented by pixel values of 1 with a background of 0 s. This skeleton is multiplied by the distance map to obtain pixel values of only fiber radii. Radii of fibers are averaged for each individual fiber and a normal distribution of fiber diameters can be obtained for each image. Yield per image was calculated by counting the connectivity of fibers between pillars, then dividing by the total possible connections in an image.

Supporting Information Available: A file containing the image analysis script written in MATLAB code, fiber formation movie, and figures showing the individual frames of interest of the fiber movie, optical profilometry height profile of pillar array, and data for images of fibers at different pillar spacings. This material is available free of charge via the Internet at http://pubs.acs.org.

References and Notes

(1) Merlo, J. A.; Frisbie, C. D. *J. Polym. Sci., Part B: Polym. Phys.* **2003**, *41*, 2674–2680.

(2) Pinto, N. J.; Johnson, A. T.; MacDiarmid, A. G.; Mueller, C. H.; Theofylaktos, N.; Robinson, D. C.; Miranda, F. A. *Appl. Phys. Lett.* **2003**, *83*, 4244–4246.

(3) Stan, M. R.; Franzon, P. D.; Goldstein, S. C.; Lach, J. C.; Ziegler, M. M. *Proc. IEEE* **2003**, *91*, 1940–1957.

(4) Rathfon, J. M.; AL-Badri, Z. M.; Shunmugam, R.; Berry, S. M.; Pabba, S.; Keynton, R. S.; Cohn, R. W.; Tew, G. N. *Adv. Funct. Mater.* **2009**, *19*, 689–695.

(5) Wang, X.; Drew, C.; Lee, S.-H.; Senecal, K. J.; Kumar, J.; Samuelson, L. A. *J. Macromol. Sci.: Part A* **2002**, *39*, 1251–1258.

(6) Wang, X. Y.; Drew, C.; Lee, S. H.; Senecal, K. J.; Kumar, J.; Samuelson, L. A. *Nano Lett.* **2002**, *2*, 1273–1275.

(7) Liu, H. Q.; Edel, J. B.; Bellan, L. M.; Craighead, H. G. *Small* **2006**, *2*, 495–499.

(8) Tong, L. M.; Gattass, R. R.; Ashcom, J. B.; He, S. L.; Lou, J. Y.; Shen, M. Y.; Maxwell, I.; Mazur, E. *Nature* **2003**, *426*, 816–819.

(9) Chou, S. Y.; Zhuang, L. *J. Vac. Sci. Technol. B* **1999**, *17*, 3197–3202.

(10) Huang, Y.; Duan, X. F.; Wei, Q. Q.; Lieber, C. M. *Science* **2001**, *291*, 630–633.

(11) Whitesides, G. M.; Grzybowski, B. *Science* **2002**, *295*, 2418–2421.

(12) Martin, C. R. *Science* **1994**, *266*, 1961–1966.

(13) Tao, S. L.; Desai, T. A. *Nano Lett.* **2007**, *7*, 1463–1468.

(14) Vandyke, L. S.; Martin, C. R. *Langmuir* **1990**, *6*, 1118–1123.

(15) Bognitzki, M.; Czado, W.; Frese, T.; Schaper, A.; Hellwig, M.; Steinhart, M.; Greiner, A.; Wendorff, J. H. *Adv. Mater.* **2001**, *13*, 70–72.

(16) Dersch, R.; Steinhart, M.; Boudriot, U.; Greiner, A.; Wendorff, J. H. *Polym. Adv. Technol.* **2005**, *16*, 276–282.

(17) Jarusuwannapoom, T.; Hongroijanawiwat, W.; Jitjaicham, S.; Wannatong, L.; Nithitanakul, M.; Pattamaprom, C.; Koombhongse, P.; Rangkupan, R.; Supaphol, P. *Eur. Polym. J.* **2005**, *41*, 409–421.

(18) Li, D.; Wang, Y. L.; Xia, Y. N. *Nano Lett.* **2003**, *3*, 1167–1171.

(19) Li, D.; Xia, Y. N. *Adv. Mater.* **2004**, *16*, 1151–1170.

(20) Sun, Z. C.; Zussman, E.; Yarin, A. L.; Wendorff, J. H.; Greiner, A. *Adv. Mater.* **2003**, *15*, 1929–1932.

(21) Sundaray, B.; Subramanian, V.; Natarajan, T. S.; Xiang, R. Z.; Chang, C. C.; Fann, W. S. *Appl. Phys. Lett.* **2004**, *84*, 1222–1224.

(22) Zhang, D.; Chang, J. *Nano Lett.* **2008**, *8*, 3283–3287.

(23) Zussman, E.; Theron, A.; Yarin, A. L. *Appl. Phys. Lett.* **2003**, *82*, 973–975.

(24) Berry, S. M.; Harfenist, S. A.; Cohn, R. W.; Keynton, R. S. *J. Micromech. Microeng.* **2006**, *16*, 1825–1832.

(25) Harfenist, S. A.; Cambron, S. D.; Nelson, E. W.; Berry, S. M.; Isham, A. W.; Crain, M. M.; Walsh, K. M.; Keynton, R. S.; Cohn, R. W. *Nano Lett.* **2004**, *4*, 1931–1937.

(26) Nain, A. S.; Wong, J. C.; Amon, C.; Sitti, M. *Appl. Phys. Lett.* **2006**, *89*, 183105.

(27) Ondarcuhu, T.; Joachim, C. *Europhys. Lett.* **1998**, *42*, 215–220.

(28) Pabba, S.; Siclorov, A. N.; Berry, S. M.; Yazdanpanah, M. M.; Keynton, R. S.; Sumanasekera, G. U.; Cohn, R. W. *ACS Nano* **2007**, *1*, 57–62.

(29) Pabba, S.; Yazdanpanah, M. M.; Fasciotto, B. H.; Dobrokhotov, V. V.; Rathfon, J. M.; Tew, G. N.; Cohn, R. W. *Soft Matter* **2009**, *5*, 1378–1385.

(30) Jeong, H. E.; Lee, S. H.; Kim, P.; Suh, K. Y. *Nano Lett.* **2006**, *6*, 1508–1513.

(31) Stafford, C. M.; Roskov, K. E.; Epps, T. H.; Fasolka, M. J. *Rev. Sci. Instrum.* **2006**, *77*.

(32) Smith, A. P.; Douglas, J. F.; Meredith, J. C.; Amis, E. J.; Karim, A. *Phys. Rev. Lett.* **2001**, *8701*, 015503.

(33) Smith, A. P.; Sehgal, A.; Douglas, J. F.; Karim, A.; Amis, E. J. *Macromol. Rapid Commun.* **2003**, *24*, 131–135.

(34) Meredith, J. C.; Karim, A.; Amis, E. J. *Macromolecules* **2000**, *33*, 5760–5762.

(35) Chattopadhyay, S.; Meredith, J. C. *Meas. Sci. Technol.* **2005**, *16*, 128–136.

(36) Meredith, J. C.; Smith, A. P.; Karim, A.; Amis, E. J. *Macromolecules* **2000**, *33*, 9747–9756.

(37) Crosby, A. J.; Fasolka, M. J.; Beers, K. L. *Macromolecules* **2004**, *37*, 9968–9974.

(38) Lee, J. Y.; Crosby, A. J. *Macromolecules* **2005**, *38*, 9711–9717.

(39) Brenn, G.; Liu, Z. B.; Durst, F. *Atomization Sprays* **2001**, *11*, 49–84.

(40) Brochard-Wyart, F.; Daillant, J. *Can. J. Phys.* **1990**, *68*, 1084–1088.

(41) Dalnoki-Veress, K.; Nickel, B. G.; Roth, C.; Dutcher, J. R. *Phys. Rev. E* **1999**, *59*, 2153–2156.

(42) Roth, C. B.; Deh, B.; Nickel, B. G.; Dutcher, J. R. *Phys. Rev. E* **2005**, *72*, 021802.

(43) Xavier, J. H.; Pu, Y.; Li, C.; Rafailovich, M. H.; Sokolov, J. *Macromolecules* **2004**, *37*, 1470–1475.

(44) The shape and roughness of pillar edges is important in the formation of holes and subsequently fibers, thus characterization of the pillars is given in Figure S2. In this study, the pillars were found to be sufficiently smooth and roughness did not have a significant effect, thus pillar edge dewetting did not occur. This is evidenced by the formation of the majority of holes in random locations on the film.

(45) Volodin, P.; Kondyurin, A. *J. Phys. D: Appl. Phys.* **2008**, *41*, 065306.

(46) Volodin, P.; Kondyurin, A. *J. Phys. D: Appl. Phys.* **2008**, *41*, 065307.

(47) Debregeas, G.; de Gennes, P. G.; Brochard-Wyart, F. *Science* **1998**, *279*, 1704–1707.

(48) Debregeas, G.; Martin, P.; Brochardwyart, F. *Phys. Rev. Lett.* **1995**, *75*, 3886–3889.

(49) Anna, S. L.; McKinley, G. H. *J. Rheol.* **2001**, *45*, 115–138.

(50) McKinley, G. H., Visco-elasto-capillary thinning and break-up of complex fluids. In *Rheology Reviews*, Binding, D. M., Walters, K., Eds. The British Society of Rheology: Aberystwyth, U.K., 2005; pp 1−48.

(51) Shin, E. H.; Cho, K. S.; Seo, M. H.; Kim, H. *Macromol. Res.* **2008**, *16*, 314–319.

(52) Ziabari, M.; Mottaghitalab, V.; Haghi, A. K. *Korean J. Chem. Eng.* **2008**, *25*, 905–918.

(53) Ziabari, M.; Mottaghitalab, V.; McGovern, S. T.; Haghi, A. K. *Nanoscale Res. Lett.* **2007**, *2*, 597–600.

(54) A sliding neighborhood operation is a function that operates pixel-by-pixel through an image, using an algorithm to determine the new pixel value. In this case pixels corresponding to intersections, objects, or discontinuities (pixels having three-point connectivity) are deleted from the image. This operation allows us to separate branched or connected fibers in the analysis.

(55) Gonzalez, R. C.; Woods, R. E., *Digital Image Processing*. 2nd ed.; Prentice Hall: Englewood Cliffs, NJ, 2001.

(56) Reiter, G. *Phys. Rev. Lett.* **1992**, *68*, 75–78.

(57) Reiter, G. *Langmuir* **1993**, *9*, 1344–1351.